PLOS Computational Biology

RESEARCH ARTICLE

Emergence of multifrequency activity in a laminar neural mass model

Raul de Palma Aristides[1*], **Pau Clusella**[2], **Roser Sanchez-Todo**[3,4], **Giulio Ruffini**[4], **Jordi Garcia-Ojalvo**[1]

1 Department of Medicine and Life Sciences, Universitat Pompeu Fabra, Barcelona, Spain, **2** Department of Mathematics, Universitat Politècnica de Catalunya, Manresa, Spain, **3** Center of Brain and Cognition, Universitat Pompeu Fabra, Barcelona, Spain, **4** Brain Modeling Department, Neuroelectrics, Barcelona, Spain

* rauldepalma@ifisc.uib-csic.es

OPEN ACCESS

Citation: de Palma Aristides R, Clusella P, Sanchez-Todo R, Ruffini G, Garcia-Ojalvo J (2026) Emergence of multifrequency activity in a laminar neural mass model. PLoS Comput Biol 22(4): e1014022. https://doi.org/10.1371/journal.pcbi.1014022

Editor: Boris S. Gutkin, École Normale Supérieure, College de France, CNRS, FRANCE

Received: June 18, 2025

Accepted: February 15, 2026

Published: April 3, 2026

Data availability statement: The codes to reproduce the main results is publicly available (https://github.com/dsb-lab/LaNMM).

Funding: Work supported by the 2024 ICREA Academy program (project 2024 ICREA 0167, Departament de Recerca i Universitats,

Abstract

Neural mass models (NMMs) aim to capture the principles underlying mesoscopic neural activity representing the average behavior of large neural populations in the brain. Recently, a biophysically grounded laminar NMM (LaNMM) has been proposed, capable of generating coupled slow and fast oscillations resulting from interactions between different cortical layers. This concurrent oscillatory activity provides a mechanistic framework for studying information processing mechanisms and various disease-related oscillatory dysfunctions. We show that this model can exhibit periodic, quasiperiodic, and chaotic oscillations. Additionally we demonstrate, through bifurcation analysis and numerical simulations, the emergence of rhythmic activity and various frequency couplings in the model, including delta-gamma, theta-gamma, and alpha-gamma couplings. We also examine how alterations linked with Alzheimer's disease impair the model's ability to display multifrequency activity. Furthermore, we show that the model remains robust when coupled to another neural mass. Together, our results offer a dynamical systems perspective of the laminar NMM model, thereby providing a foundation for future modeling studies and investigations into cognitive processes that depend on cross-frequency coupling.

Author summary

Understanding how the brain generates and coordinates rhythms across different layers is essential for uncovering the mechanisms underlying perception, memory, and cognition. In this work, we analyze a previously developed model of mesoscopic brain activity that simulates the layered structure of the cortex and its ability to produce coupled slow and fast neural oscillations. Using tools from dynamical systems theory, we reveal how the model gives rise to a rich repertoire of dynamical patterns—including periodic, quasiperiodic, and chaotic

Generalitat de Catalunya). RdPA, PC, RS-T, GR and JG-O are supported by the European Commission under European Union's Horizon 2020 research and innovation programme Grant Number 101017716 (Neurotwin). PC was also financially supported by the project PID2024-155942NB-I00 funded by MICIU/AEI/10.13039/501100011033 and ERDF, UE. JG-O was also financially supported by the Spanish Ministry of Science and Innovation, the Spanish State Research Agency and FEDER (Project Reference No. PID2024-160263NB-I00), and the European Research Council (ERC Synergy CeLEARN-101167121). GR and RS-T are also funded by the European Research Council (ERC Synergy Galvani) under the European Union's Horizon 2020 research and innovation program Grant Number 855109. The funders had no role in study design, data collection and analysis, decision to publish, or preparation of the manuscript.

Competing interests: I have read the journal's policy and the authors of this manuscript have the following competing interests: GR is a co-founder of Neuroelectrics, a Company that manufactures tES and EEG technology. The remaining authors don't have any conflict of interest.

activity—through the coexistence of multiple oscillatory modes. We also investigate how pathological changes, such as those linked to Alzheimer's disease, alter the model's dynamics and impair its capacity to sustain complex cross-frequency interactions. Finally, we show that the model remains stable when connected to another brain region, highlighting its robustness. Our findings provide a deeper understanding of how multifrequency neural rhythms may emerge, how they might break down in disease, and how this modeling framework can inform both future theoretical studies and the development of new brain models.

1 Introduction

Oscillations are ubiquitous in the brain [1]. These rhythmic or repetitive patterns of electrical activity emerge from the firing of individual neurons, reflecting the synchronized activity of neuronal ensembles, and are therefore the result of the interplay between different scales: microscopic (single neurons), mesoscopic (local groups of neurons), and macroscopic (across brain regions) [2,3]. The frequencies in which mammalian neuronal networks oscillate span four orders of magnitude, ranging from 0.05 Hz to 500 Hz, with this diversity arising from neuron and synapse properties, their interactions, and the circuit motifs that they form [4].

Neural mass models (NMMs) can capture the mesoscopic dynamics of ensembles of neurons as nonlinear oscillators [5–9]. In this formalism, a population is typically characterized by its average firing rate, membrane potential, as well as the characteristics of synapses through which it connects to other populations (time constant and amplitude of post-synaptic potentials, or PSPs). Although limited, these models have been instrumental in advancing our understanding of brain rhythms, successfully replicating brain activity patterns observed through electrophysiological and neuroimaging techniques [10–24].

In this paper we focus on the emergence of multifrequency coupling in the recently introduced *laminar* NMM (LaNMM) [25], an extended NMM that includes the layered structure of the cortex and describes the frequency bias and coupling between layers. Such a phenomenon appears to be crucial for brain activity, and plays a role in cognitive functions [26–33]. Recent work with the LaNMM has shown how this model can be used to implement gating and predictive coding elements [34] and cooperation/competition across brain regions [35]. Frequency bias is observed across cortical layers, with different frequency bands contributing to distinct aspects of neural processing and communication [27,36,37]. For example, during a memory task, macaques exhibit high-frequency activity in superficial layers and low-frequency activity in deep layers. Moreover, the phase and amplitude of deep-layer low-frequency oscillations influence the phase and amplitude of superficial gamma dynamics, highlighting the intricate interplay between frequencies across cortical layers [37].

From the dynamical point of view, this is the result of the interaction of different nonlinear oscillators, each one with a different natural frequency. In turn, this frequency depends on the intrinsic properties of each neuronal population, such as

the synaptic characteristics of neurons that make up the population and the connectivity between them. Hence, when we consider the interaction between different populations, we have to take into account the tendency of each population to oscillate in its preferred frequency. From this interplay, many interesting and complex phenomena emerge, including, multifrequency coexistence, chaos and cross-frequency coupling [38–43].

The LaNMM combines two well-known NMMs: the Jansen-Rit model [7,8,44] and a model implementing the pyramidal-interneuron network gamma (PING) mechanism [5,45–48]. The first model, consisting of a population of pyramidal neurons coupled to two other populations, is responsible for sustaining lower frequencies and is associated with deeper cortical layers. The latter model includes a pyramidal and an interneuron population, and generates faster rhythms in the gamma band. Finally, inputs to the two pyramidal populations are added to simulate signals from other cortical regions. By integrating these elements, the LaNMM elegantly displays cortical oscillations across different frequency bands [22,25], and has been used to model phenomena including effects of serotonergic psychedelics [49], oscillatory changes in Alzheimer's disease [34,50], predictive coding mechanisms [34], and cooperative vs. competitive interactions [35]. In particular, the last two studies build on the cross-frequency coupling characteristics of the LaNMM.

Here, we analyze the LaNMM's ability to display multifrequency dynamics as a function of the (constant) inputs of its pyramidal populations. Specifically, we conduct a bifurcation analysis of the model with respect to changes in the input parameters. We show that in addition to the alpha-gamma coupling described in [22,25,34,35], the model is also capable of generating delta-gamma and theta-gamma coupling, which, to our knowledge, has not been previously reported for other NMMs. Our analysis reveals that the parameter space of external inputs contains a large region of quasiperiodicity, where multifrequency coupling emerges due to the coexistence of two unstable limit cycles associated with the two components of the model: the Jansen-Rit and the PING. Additionally, we examine how alterations associated with Alzheimer's disease impair this capability, by analyzing their impact on the bifurcation diagram and how they reshape the regions where the system exhibits multifrequency activity. Furthermore, we demonstrate that the model remains robust when coupled to other neural masses.

2 Methods

2.1 Laminar neural mass model

Neural mass models are lumped mathematical descriptions of neuronal activity that aim to mimic the behavior of populations of neurons with a small number of differential equations. Our main object of study is the LaNMM, first proposed in [22,25], which consists of five interconnected populations of neurons, each representing a different cell type:

- Pyramidal cells located at deep cortex layers (P_1).
- Pyramidal cells located at superficial layers (P_2).
- Fast inhibitory parvalbumin-positive cells (PV).
- Slow inhibitory somatostatin-expressing cells (SST).
- Excitatory spiny stellate cells (SS).

Additionally, we consider two generic external inputs targeting P_1 and P_2 that represent incoming inputs from other neuronal populations. Fig 1 illustrates the model and the connectivity between these populations. Excitatory synapses, mediated by AMPA neurotransmitters, are represented as triangles, while inhibitory synapses, mediated by GABA neurotransmitters, are shown as circles.

The dynamics of each population and their interactions are modeled following heuristic principles proposed by seminal studies in the field [5,7,51,52]. First, the average axonal pulses originated in one population (with average firing rate $r(t)$) produce an average postsynaptic potential (PSP) $y(t)$ via a linear convolution [52]:

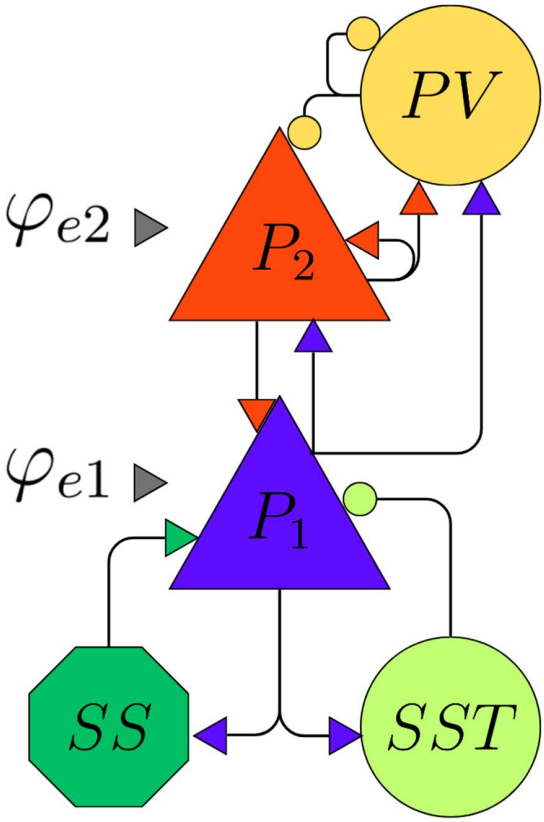

Fig 1. Illustration of the neuronal populations in the exact neural mass model and the connectivity between them. Blue triangles represent the excitatory neuron population, while orange circles denote the inhibitory population. Coupling within and between populations is weighted by the constants J_{xy}, where x and y indicate the source and target of the synapses, respectively. External inputs to the populations are denoted by I_e and I_i, for excitatory and inhibitory populations.

https://doi.org/10.1371/journal.pcbi.1014022.g001

$$y(t) = \int_{-\infty}^{\infty} h(t-t')r(t')dt' \ . \tag{1}$$

The kernel h reads:

$$h(t) = \begin{cases} Aate^{-at} & t \geq 0 \\ 0 & t < 0 \end{cases} \tag{2}$$

were parameters A, a vary depending on the effect of the modeled neurotransmitter on the postsynaptic population. For instance, while excitatory neurotransmitters cause excitatory postsynaptic potentials (EPSPs), which depolarize the postsynaptic population, inhibitory neurotransmitters cause inhibitory postsynaptic potentials (IPSPs), which have the opposite effect. Specifically, the amplitude and timescale of the postsynaptic potentials depend on the parameters A(mV), which represents the synaptic gain, and a(s-1), which is the time constant of the average PSP. Fig 2a shows the three different PSPs captured by Eq. (2) for individual populations (i.e., in the absence of coupling), one for excitatory synapses (mediated by AMPA neurotransmitter, *AMPA*, blue line) and the other two for inhibitory synapses (mediated by slow and fast GABA neurotransmitter, G_s and G_f, green and yellow lines respectively).

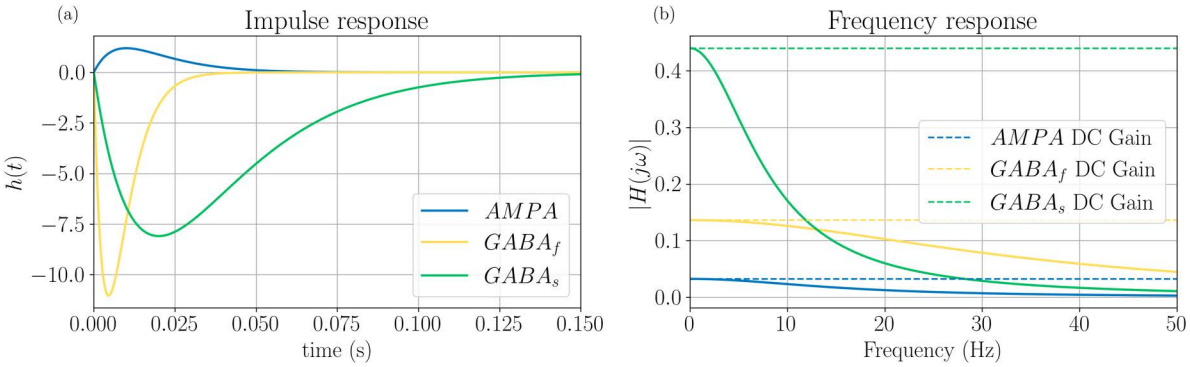

Fig 2. The three types of *h* kernels present in the LaNMM lead to different post-synaptic potentials. The PSP amplitudes and decay time are governed by the parameters *A* and *a*, respectively. The right hand side displays the frequency response of the filters.

https://doi.org/10.1371/journal.pcbi.1014022.g002

In Fig 2, the strongest PSPs are generated by GABAergic interneurons, with PV neurons (with $GABA_f$) responding the fastest and SST neurons (with $GABA_s$) the slowest. The IPSPs have a larger amplitude than the EPSPs, due to inhibitory neurons establishing synapses closer to the cell body of postsynaptic cells [7,53]. The frequency response associated with each *h*-block, shown in Fig 2b, is obtained as the Fourier transform of $h(t)$ (Eq. (2)), which yields $H(j\omega) = \frac{Aa}{(a+j\omega)^2}$ [54]. This expression describes how each synapse amplifies or attenuates signals across different frequencies. AMPA is the least responsive of all synapses, with a weaker response at higher frequencies. In contrast, fast GABA shows more responsiveness at higher frequencies, i.e., it is more sensitive to fast oscillations and rapid signals, which is typical for fast inhibitory synapses.

A second key ingredient of the modeling is a nonlinear function $\sigma(v)$ that relates the average membrane potential (v) to an average firing rate [55]:

$$\sigma(v(t)) = \frac{2\varphi_0}{1 + e^{r(v_0 - v(t))}}\ , \tag{3}$$

where φ_0 is the half maximal firing rate of the targeted population, v_0 is the value of the potential when φ_0 is achieved, and r determines the steepness of the sigmoid at the threshold (v_0, φ_0).

Combining Eq. (1) with the specific form of the synaptic kernel Eq. (2), the average membrane potential $y(t)$ in response to an input $\sigma(v(t))$ can be written as a convolution with $h(t)$. From linear systems theory and the properties of the synaptic kernel, one can obtain the following equivalent second-order differential equation for $y(t)$ [56]:

$$\frac{d^2y(t)}{dt^2} + 2a\frac{dy(t)}{dt} + a^2y(t) = Aa\,\sigma(v(t))\ . \tag{4}$$

Using Eq. (4) and considering the connectivity scheme described in Fig 1, the system of equations governing the model is given by

$$\dot{y}_1 = y_6 \tag{5a}$$

$$\dot{y}_6 = a_A A_A \sigma_{P_1}(C_1 y_2 + C_2 y_3 + C_3 \varphi_{e1} + C_{11} y_4) - 2a_A y_6 - a_A^2 y_1 \tag{5b}$$

$$\dot{y}_2 = y_7 \tag{5c}$$

$$\dot{y}_7 = a_A A_A \sigma_{SS}(C_4 y_1) - 2a_A y_7 - a_A^2 y_2 \tag{5d}$$

$$\dot{y}_3 = y_8 \tag{5e}$$

$$\dot{y}_8 = a_{G_s} A_{G_s} \sigma_{SST}(C_5 y_1) - 2a_{G_s} y_8 - a_{G_s}^2 y_3 \tag{5f}$$

$$\dot{y}_4 = y_9 \tag{5g}$$

$$\dot{y}_9 = a_A A_A \sigma_{P_2}(C_6 y_4 + C_7 y_5 + C_8 \varphi_{e2} + C_{12} y_1) - 2a_A y_9 - a_A^2 y_4 \tag{5h}$$

$$\dot{y}_5 = y_{10} \tag{5i}$$

$$\dot{y}_{10} = a_{G_f} A_{G_f} \sigma_{PV}(C_9 y_4 + C_{10} y_5 + C_{13} y_1) - 2a_{G_f} \dot{y}_{10} - a_{G_f}^2 y_5 \tag{5j}$$

where the description and values of the parameters are given in Table 1. In this paper we will pay particular attention to the effects that the external inputs φ_{e1} and φ_{e2} (acting upon the pyramidal populations P_1 and P_2, respectively) have on the dynamics of the system.

In the next section we present a detailed analysis of the dynamics and bifurcations of system (5).

Table 1. Description of model parameters and their standard values, as used in [22].

Parameter	Description	Value
A_s	Average synaptic gain	A_A = 3.25mV; A_{G_s} = –22mV A_{G_f} = –30mV
a_s	Time rate constant of average postsynaptic potentials	$a_A = 100s^{-1}$; $a_{G_s} = 50s^{-1}$ $a_{G_f} = 220s^{-1}$
C_s	Average number of synaptic contacts between population types	C_1 = 108, C_2 = 33.7, C_3 = 1, C_4 = 135, C_5 = 33.75, C_6 = 70, C_7 = 550, C_8 = 1, C_9 = 200, C_{10} = 100, C_{11} = 80, C_{12} = 200, C_{13} = 30.
v_0	Potential when 50% of the firing rate is achieved	6mV (except for P_2: 1mV).
φ_0	Half of the maximum firing rate	2.5 Hz
r	Slope of the sigmoid function at v_0	0.56mV^{-1}
φ_e	External input	$\varphi_{e1} = \frac{A_A}{a_A}200$, $\varphi_{e2} = \frac{A_A}{a_A}90$

https://doi.org/10.1371/journal.pcbi.1014022.t001

3 Results

3.1 Baseline dynamics of the LaNMM

In this section, we explore the dynamical properties of the system described by Eq. (5). We begin by analyzing the model's response to external inputs. Specifically, we simulate the system starting from a fixed point (with $\varphi_{e1} = \varphi_{e2} = 0$) and apply a pulse simultaneously to both P_1 and P_2 at $t = 0$. Fig 3 illustrates the *t*ime evolution of the membrane potentials of the model's two main neural populations. These observables are given by [22]:

$$v_{P_1} = C_1 y_2 + C_2 y_3 + C_{11} y_4 \tag{6}$$

$$v_{P_2} = C_6 y_4 + C_7 y_5 + C_{12} y_1. \tag{7}$$

For better visualization, we center the signals at $v = 0$ by removing their DC components, to enhance the comparison between responses. We observe differences not only in amplitude but also in the timescale of the response. P_2 exhibits a stronger response, characterized by a fast initial peak followed by damped oscillations back to the steady state. In contrast, P_1 has a significantly slower response with a smaller amplitude. These differences in response dynamics align with the intrinsic properties of these populations: P_2 has higher excitability (lower v_0) and faster intrinsic time scales due to its coupling with *PV* cells. The slower recovery of P_1 is influenced by *SST* cells, which exhibit the slowest response, as shown in Fig 2. On the other hand, the network responses shown in Fig 3 differ significantly from those observed in Fig 2, which is to be expected since populations with distinct amplitudes and time constants now interact. We will revisit this response when analyzing the stability of the fixed point of the system in the next section.

As previously mentioned, a key feature of this neural mass model is its ability to sustain distinct oscillatory frequencies across different populations, particularly in the alpha and gamma bands. This behavior is illustrated in Fig 4, where the time evolution of the membrane potentials of populations P_1 and P_2 are shown in Fig 4a and 4b, respectively, for $\varphi_{e1} = 200$ and $\varphi_{e2} = 90$ as in the model in [22]. While both populations exhibit rhythmic activity, their temporal dynamics differ significantly, with P_1 oscillating at a lower frequency, around 10 Hz (alpha range), compared to the faster oscillations of P_2, around 40 Hz (gamma range).

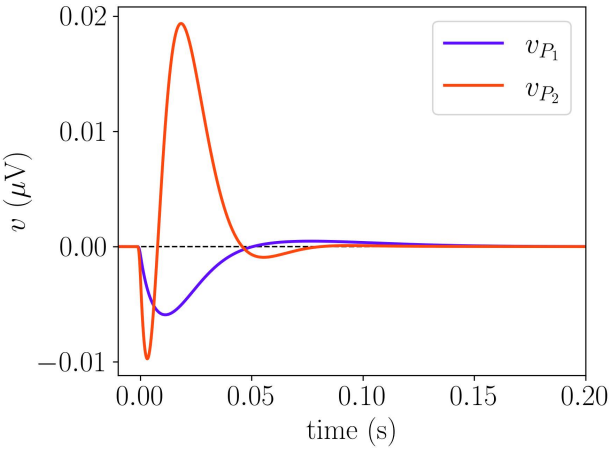

Fig 3. Response of the model for a pulse of 1 ms delivered to P_1 and P_2 simultaneously. Parameters values as in Table 1, with $\varphi_{e1} = 0$ and $\varphi_{e2} = 0$.

https://doi.org/10.1371/journal.pcbi.1014022.g003

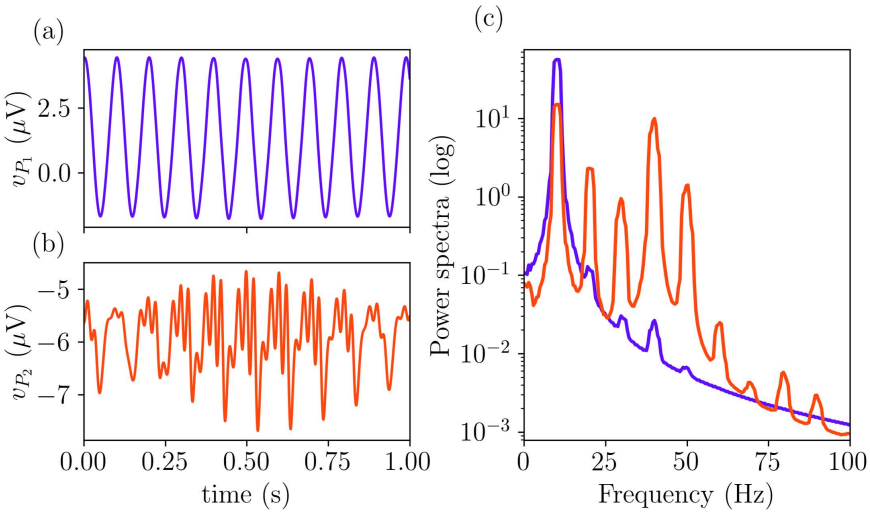

Fig 4. Time evolution of the membrane potentials of *P*1 (a) and P_2 (b) with the respective power spectra shown in panel (c). Parameters values as in Table 1 with φ_{e1} = 200 φ_{e2} = 90.

https://doi.org/10.1371/journal.pcbi.1014022.g004

To further characterize these differences, Fig 4c displays the power spectra of each signal. The two curves are plotted using the same colors as the corresponding time series in Fig 4a and 4b. This analysis confirms that while both populations share a strong α component around 10 Hz, P_2 exhibits pronounced γ-band activity at around 40 Hz. The shared α rhythm enables cross-frequency coupling, where γ oscillations in P_2 may be modulated by the phase of the α rhythm. These features were explicitly introduced into the model to ensure a representation of experimental results [22].

3.2 Fixed points and bifurcations

We now look for the fixed points of the system (5). To solve this system and find the fixed points, we used the continuation and analysis software AUTO-07p [57]. Fig 5a and 5b show a one-parameter bifurcation diagram obtained by varying the external input of the pyramidal population P_1, φ_{e1}, while keeping φ_{e2} = 0, in terms of the observables v_{P_1} (a) and v_{P_2} (b).

Stable (unstable) fixed points are shown in dark (light) grey, together with the amplitude of stable (unstable) periodic solutions in dark (light) colors. The local stability of periodic solutions is given by the Floquet multipliers, which determine if perturbations to such solutions grow or decay. The bifurcations related to the emergence of oscillatory dynamics are marked by vertical lines in Fig 5a and 5b. These figures show that the system has one stable fixed point for small inputs to P_1. This stable fixed point, located on the lower branch, has three distinct pairs of complex eigenvalues and two real eigenvalues. This implies that when perturbed, the system's response will be a combination of oscillatory behavior and exponential decay toward the steady state, in line with the results in Fig 3.

Increasing φ_{e1} leads the system through a saddle-node on an invariant circle (SNIC) bifurcation at $\varphi_{e1} \approx 107$, as two fixed points collapse and a stable invariant cycle appears. Notice that this bifurcation is also encountered in the single Jansen's model [44]. The amplitude of the oscillations decreases and the frequency increases after the system passes through two fold (saddle-node) bifurcations of limit-cycles ($FLC_{1,2}$) at $\varphi_{e1} \approx 159$, which are too close to each other to be seen separately in the diagram [58]. This oscillatory activity vanishes at a supercritical Hopf bifurcation (HB_1^+) at $\varphi_{e1} \approx 367$. Increasing φ_{e1} leads to a second supercritical Hopf bifurcation (HB_2^+) at $\varphi_{e1} \approx 457$ and to a second invariant cycle, which has a higher frequency and a much smaller amplitude (in P_1) than the first one. In what follows, we analyze the oscillation dynamics of the model part by part.

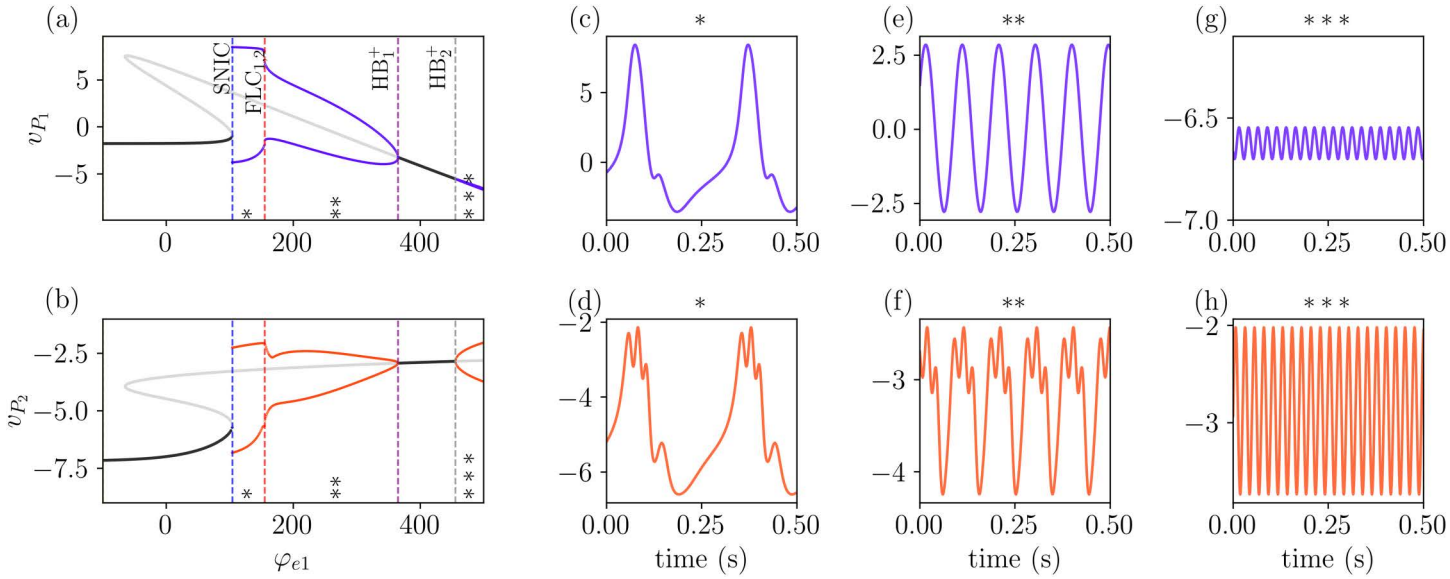

Fig 5. Bifurcation diagram of the system showing the fixed points and the amplitude of oscillatory solutions for v_{P1} and v_{P2} in panels (a,b), with $\varphi_{e2} = 0$. Stable (unstable) fixed points are shown in dark (light) grey. Increasing the external input (φ_{e1} leads to the emergence of oscillatory activity through a SNIC bifurcation (see text). Further increases in φ_{e1} result in a Fold of Limit Cycle (FLC) bifurcation, followed by a sequence of supercritical Hopf bifurcations (HB⁺). Different oscillatory regimes are marked by asterisks (∗) and are plotted in panels **(c,d)**, (e,f) and **(g,h)**. Although the three oscillatory regimes are periodic, each one exhibits a different main frequency: in **(c-d)** $\theta \approx 4$ Hz, in **(e-f)** $\alpha \approx 10$ Hz, and in **(g-h)** $\gamma \approx 40$ Hz. For (∗), $\varphi_{e1} = 125$; for (∗∗), $\varphi_{e1} = 250$; and for (∗), $\varphi_{e1} = 500$. The remaining parameter values are as given in Table 1.

https://doi.org/10.1371/journal.pcbi.1014022.g005

We divide Fig 5a and 5b into three different regions marked with *'s, each one associated with different oscillatory behaviors exhibited by the system. Each one of them is shown in Fig 5c and 5g for v_{P1} and 5d and 5h for v_{P2}. The activity in all three regions is periodic and stable, as confirmed by the corresponding Floquet multipliers obtained with AUTO-07p [57].

In the region labeled as (*) in Fig 5a, between the SNIC and the FLC bifurcations, the system displays theta rhythmic activity with frequency ≈ 4 Hz, as shown in 5c and 5d. It is important to notice that although the main frequency of both signals is the same, v_{P2} (5d) exhibits a fast oscillation on top of the main one. In the region between FLC and the HB_1^+, labeled as (**) in Fig 5a, the system exhibits alpha rhythmic activity with frequency ≈ 10 Hz, and similarly to the region before, v_{P2} shows a fast oscillation for v_{P2} superimposed on the slower one, as shown in Fig 5e and 5f.

The results described above reveal that not only v_{P2} exhibits a fast oscillation, but this oscillation is locked with the phase of v_{P1}. This can be understood by considering the two parts of the model, the Jansen-Rit and the PING, as two coupled oscillators. In regions * and **, the Jansen-Rit drives the PING activity. This driving is modulated by the σ_{P_2} function (Eq. (3)), which increases considerably as v_{P_2} approaches $v_0 = 1$.

Lastly, gamma rhythmic activity is observed in the region labeled as ***, after the HB_2^+ bifurcation, with frequency ≈ 40 Hz, as shown in Fig 5g and 5h. This can be explained by analyzing the dynamics of the single Jansen's model [44]. For this input value, the system does not oscillate; instead, it settles into a stable fixed point. In contrast, the PING model exhibits oscillations. As a result, the Jansen-Rit model is being driven by the PING model, but its inherent dynamics suppress the oscillations, trying to pull the system toward its fixed point and hence leading to small amplitudes in the P_1 oscillations. Summarizing, for $\varphi_{e2} = 0$ the system does not exhibit simultaneously multifrequency activity, in the sense that both v_{P1} and v_{P2} share a single dominant frequency. Because the system is deterministic and produces discrete spectral lines characteristic of periodic or quasiperiodic dynamics, this frequency is reliably identified by the PSD peak without the

need for aperiodic-background corrections. That is, only one main frequency is observed across both populations. In the following, we analyze how increasing φ_{P2} alters this scenario and can lead to the emergence of distinct dominant frequencies for each population.

The effect of a non-zero input in the P_2 population is shown in Fig 6, which presents different bifurcation diagrams with increasing φ_{e2} from left to right, using the same color scheme as Fig 5. As we see in the first column (Fig 6a and 6d), increasing the value of φ_{e2} to 20 makes little difference in the position of the first bifurcations (SNIC, FLC, and HB_1^+). However, the bifurcation point HB_2^+ has moved significantly to the left. As we increase $\varphi_{e2} = 40$, we notice a change in the sequence of bifurcations. Now, after the FLC bifurcations, the system goes through a subcritical Hopf bifurcation HB_2^- (the former HB_2^+ bifurcation becomes subcritical when it crosses HB_1^+), which leads to an unstable periodic solution.

Notice that from this point on, until the system reaches HB_1^+, there is an overlap between former regions ** and ***, sustaining alpha and gamma rhythms, respectively. Between these two bifurcations, we notice another one, namely a torus (or secondary Hopf) bifurcation, TR (yellow dashed line in Fig 6c-f). Before the TR bifurcation, the unstable inner limit cycle repels the trajectories that are attracted by the outer stable limit cycle (better visualized in Fig 6d). The crossing of the TR bifurcation leads to the loss of the stability of the periodic solution, leading to the emergence of the quasiperiodic behavior. In this regime, the trajectories are attracted to a two-dimensional torus and repelled from the inner limit cycle. For $\varphi_{e2} = 90$, the scenario remains qualitatively similar, with both HB_2^- and TR shifting significantly to the left, which enables a larger region of overlap between the different limit cycles. Notice that the values used in Fig 4 lie on the region slightly after the TR bifurcation.

The two-parameter bifurcation diagram ($\varphi_{e1} \times \varphi_{e2}$) shown in Fig 7 gives us a better view of how the bifurcation points change for different parameter values. We see that except for the TR bifurcation, the other bifurcations are not significantly affected by the increase of φ_{e2}, in agreement with the results of Fig 6. To better understand how the bifurcation structure affects the frequency of the signals v_{P_1} and v_{P_2}, we numerically solved Eq. (5) varying φ_{e1} and φ_{e2}, with results in presented in Fig 7b and 7c. For clarity, the frequency range between 12 and 30Hz is omitted, since the model does not produce significant spectral components in this band. By comparing the main frequencies of v_{P_1} and v_{P_2} (Fig 6b and 6c, respectively)

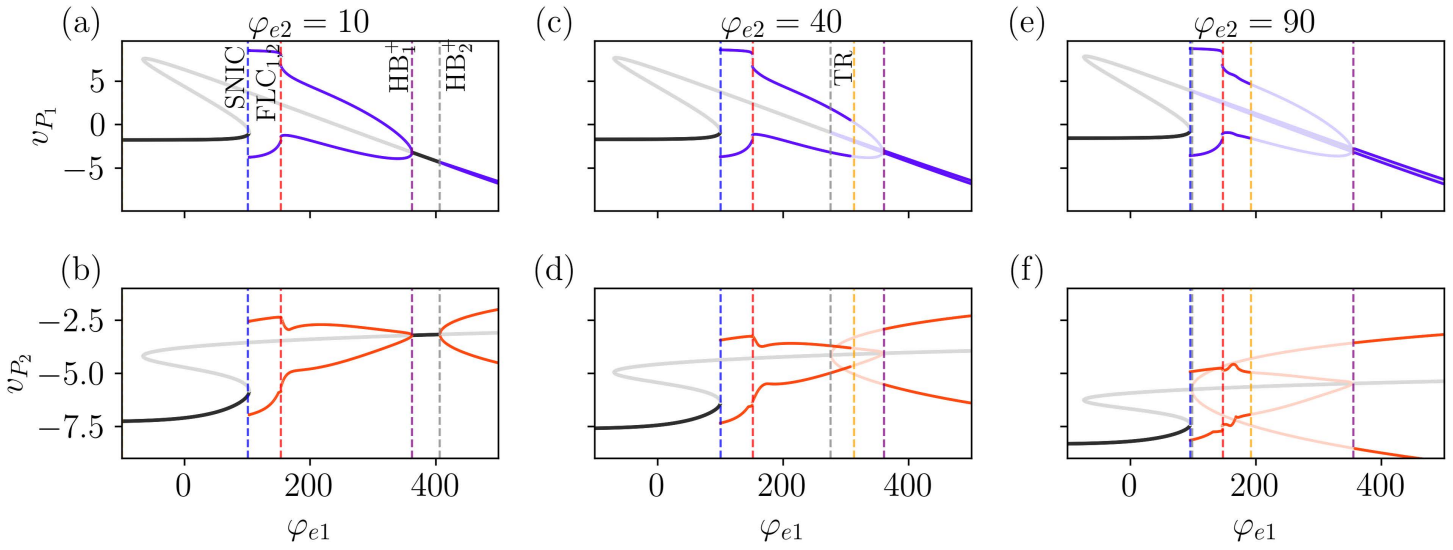

Fig 6. Effect of increasing φ_{e2} on the bifurcation diagram. Bifurcation diagrams obtained by varying φ_{e1} for different values of φ_{e2}. Increasing φ_{e2} (left to right) lowers the threshold for the second Hopf bifurcation, HB_2^+, which appears at smaller values of $\varphi e1$. Additionally, it also induces a torus bifurcation (TR). Other parameter values are given in Table 1.

https://doi.org/10.1371/journal.pcbi.1014022.g006

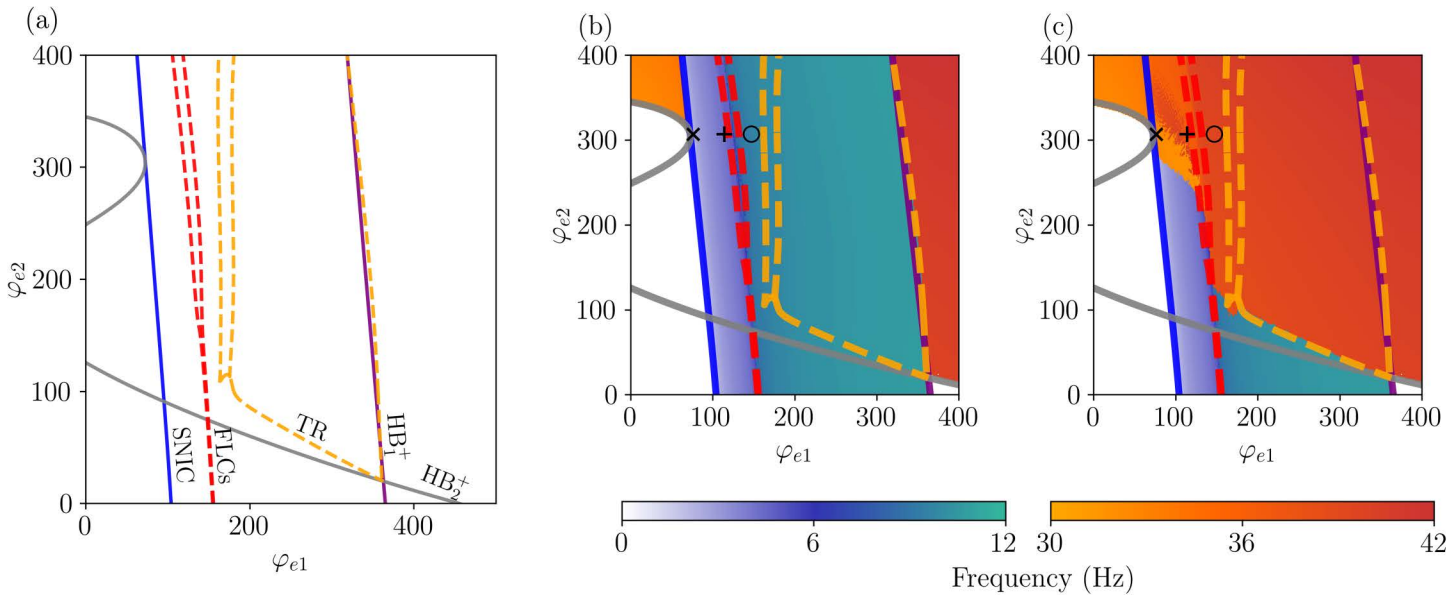

Fig 7. Bifurcation structure underlying frequency transitions and coexistence in the laminar model. (a) Two-parameter bifurcation diagram of Eq. (5), where color scheme used for bifurcations is the same as in Fig 2. Panels (b) and (c) show regions colored according to the dominant frequencies of (b) v_{P_1} and (c) v_{P_2}, highlighting the model's ability to sustain multifrequency activity depending on the combination of φ_{e1} and φ_{e2}. The area of multifrequency activity is bounded by the SNIC (blue) and HB_1^+ (purple) bifurcations. In panel (b), we observe that the dominant frequency of v_{P_1} remains robust as φ_{e2} increases. Between the SNIC and FLC bifurcations, v_{P_1} exhibits oscillations in the delta (0.5–4 Hz) and theta (4–7 Hz) ranges. As we move from the FLC to the HB_1^+ bifurcations, v_{P_1} transitions to oscillations in the alpha range (8–13 Hz). For v_{P_2} (panel c), the scenario differs. As φ_{e2} increases, the system undergoes a TR bifurcation, shifting the regime and causing the main frequency to move from the alpha range to the gamma range (> 30 Hz) between the FLC and HB_1^+ bifurcations. Additionally, in the region between the SNIC and FLC bifurcations, increasing φ_{e2} induces a change in the rhythmic activity of v_{P_2}, transitioning from delta/theta frequencies to gamma frequencies for $\varphi_{e2} > 250$. Other parameter values are given in Table 1.

https://doi.org/10.1371/journal.pcbi.1014022.g007

we verify the presence of regions where both populations display the same frequency, such as before the SNIC and after the HB_1^+ bifurcations, and also regions with multifrequency activity.

Specifically, we identify two regions of multifrequency activity. The first occurs for $\varphi_{e2} > 250$, bounded by the SNIC and FLC bifurcations. In this region, the system exhibits frequencies ranging from approximately 2.5 to 5.0 Hz in v_{P_1}, spanning both δ (0.5–4 Hz) and θ (4–8 Hz) bands, depending on the value of φ_{e1}. Concurrently, v_{P_2} displays γ band activity. The second region of multifrequency activity arises as φ_{e1} increases beyond the FLC bifurcation. Here, v_{P_1} transitions into the alpha band until it reaches the HB_1^+ bifurcation, while v_{P_2} maintains γ frequencies (above 30 Hz) after crossing the TR bifurcation. This results in a second distinct region where the two populations oscillate at separate dominant frequencies.

These different dynamics are highlighted in Fig 8, which shows the time evolution of the system at the $(\varphi_{e1}, \varphi_{e2})$ values indicated by the markers $(\times, +, \circ)$ in Fig 7. Fig 8a and Fig 8b show that δ activity is displayed by P_1, while γ activity is observed in P_2. Increasing φ_{e1} results in an increase of the frequency of v_{P_1} to the θ range, and while this component is also observed in the signal of v_{P_2}, the main frequency for this populations remains on the γ range, as shown in Fig 8c and Fig 8d. Lastly, by increasing φ_{e1} further, we show the coupling between α and γ frequencies in Fig 8e and Fig 8f. Interestingly, we notice that the amplitude of v_{P_2} which displays γ rhythm is modulated by the cycle of v_{P_1} in all three cases (δ, θ, and α rhythms).

To verify this, we quantified the phase–amplitude coupling using the method proposed by Tort et al. [59], which provides a modulation index indicating how strongly the amplitude in one frequency band is coupled to the phase in another frequency band. Specifically, we considered phases in δ (2–4 Hz), θ (4–8 Hz), and α (8–13 Hz), and amplitudes in the γ range (30–100 Hz), with signals (v_{P1}, v_{P2}) filtered using a zero-phase Butterworth band-pass filter in the corresponding

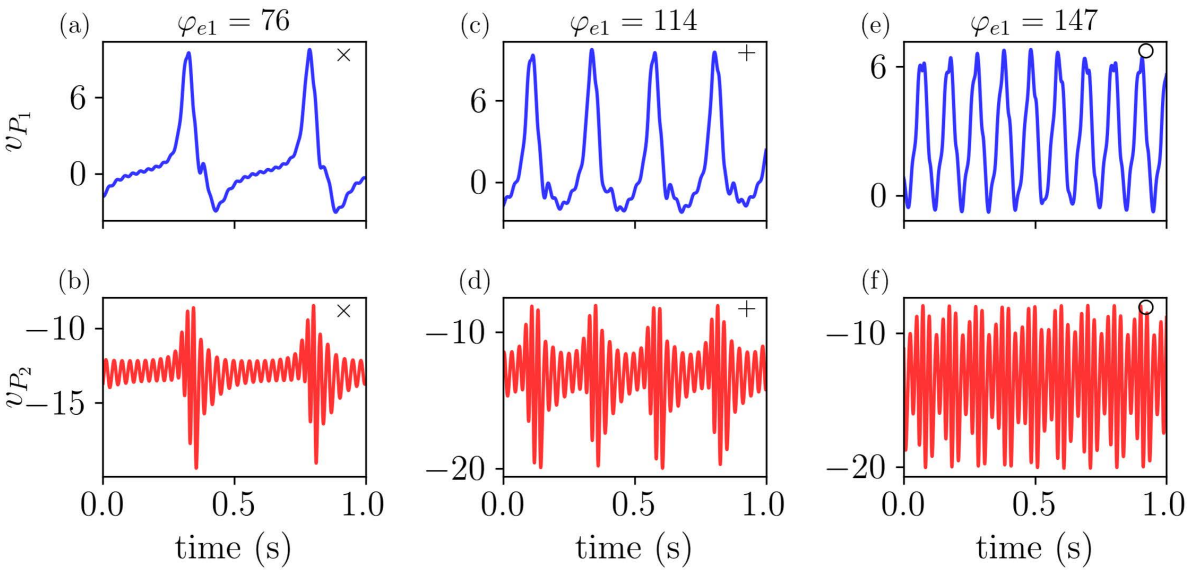

Fig 8. The model exhibits different frequency couplings depending on φ_{e1} and φ_{e2}. The time evolution of v_{P_1} and v_{P_2} is shown for the parameter values highlighted in Fig (7), illustrating: (a-b) coupling between δ and γ frequencies, (c-d) coupling between θ and γ frequencies, and (e-f) coupling between α and γ frequencies. All parameters are as listed in Table 1, except for φ_{e2} = 307.

https://doi.org/10.1371/journal.pcbi.1014022.g008

ranges. We found MI values of 0.076, 0.051, and 0.008 for the signals in Fig 8a and 8b, 8c and 8d, and 8e and 8f, respectively. For further details on the MI and the phase–amplitude coupling in the LaNMM model, we refer the reader to [59] and [34], respectively.

We further validate our results by calculating the two largest Lyapunov exponents (LEs) (see S1 Lyapunov exponents), λ_1 and λ_2, as a function of the external inputs φ_{e1} and φ_{e2}. Based on these exponents, the dynamical regimes of the system are classified and displayed in Fig 9, overlapped with the two-parameter bifurcation diagram. Together, these two values provide insight into the system's dynamics: The presence of a positive LEs signifies chaos, while negative LEs indicate steady-state dynamics. If one LE is zero, the system exhibits periodic behavior. In contrast, if the system has two zero LEs, it evolves on a two-dimensional invariant torus, indicating quasiperiodicity. As expected, both periodic and quasiperiodic dynamics are observed, with the quasiperiodic regions emerging and being enclosed by torus bifurcations. Interestingly, the system also displays chaotic dynamics in the vicinity of a complex region between FLC bifurcations for high values of φ_{e2}. Such a transition from quasiperiodic to chaotic dynamics is also known as *torus breakdown*. The presence of FLC bifurcations in this region implies the emergence and annihilation of an unstable limit cycle, which can create conditions favorable for chaotic dynamics.

It is worth noting that we did not account for aperiodic components when estimating the main frequency of signals v_{P1} and v_{P2}. For v_{P2}, where the α- and γ-range peaks can have similar amplitudes, varying parameters as in Fig 7 could lead to different dominant frequencies if the aperiodic component were included, particularly near the boundary between the low- and high-frequency regimes (dashed yellow TR and dashed red FLC lines). In such cases, incorporating the aperiodic contribution might even shift some parameter values from a low to a high dominant frequency. Part of this boundary also aligns with the transition from periodic to quasi-periodic dynamics (Fig 9), where the aperiodic component is expected to be larger. Thus, some of the apparent frequency changes across this region may partly reflect differences in the aperiodic background rather than changes in the oscillatory peak itself, a point that will be addressed in future work.

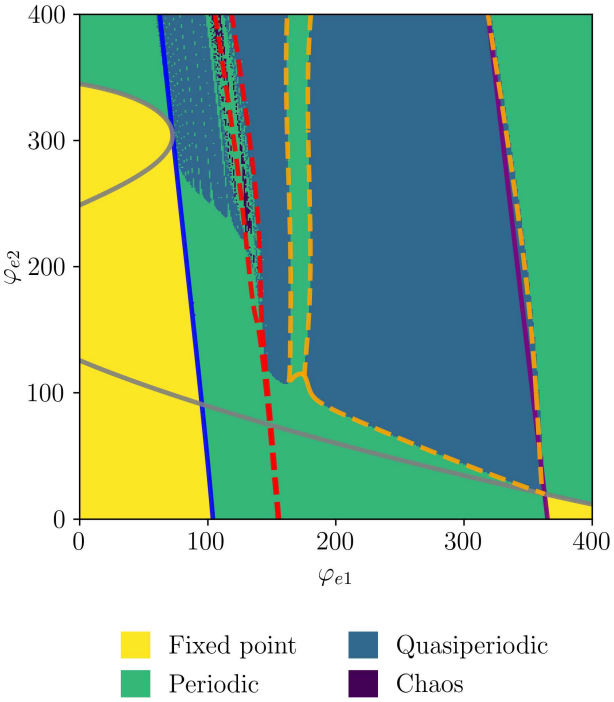

Fig 9. Two-parameter bifurcation diagram of Eq. (5) with regions colored according to the two largest Lyapunov exponents as a function of φ_{e1} and φ_{e2}. Parameters values as in Table 1. The resolution of the parameter space is 384 × 384.

https://doi.org/10.1371/journal.pcbi.1014022.g009

3.3 PV interneuron dysfunction

In this section we investigate the role of *PV* cells in the multifrequency observed in the previous sections, more specifically, we focus on reducing the coupling from *PV* to P_2, i.e., $C_7 = C_{PV\to P_2}$. Recently, this has been proposed as a mechanism to model the accumulation of amyloid-beta oligomers (AβO), which is supposed to damage the synaptic function of *PV* interneurons [50]. The accumulation of AβOs in the brain correlates with Alzheimer's disease (AD) progression, as these soluble oligomers, formed by 2–50 monomers, are believed to be the main culprits behind various neurotoxic effects leading to cognitive decline and begin forming years before clinical signs of the disease appear [48,60–63].

Fig 10 reproduces the two-parameter bifurcation diagram from Fig 7, focusing on the bifurcation that defines the coexistence of limit cycles (SNIC, HB_1^+, HB_2^+) for different values of $C_{PV\to P_2}$. For comparison, we include the case where $C_{PV\to P_2} = 550$, representing the baseline or healthy condition, which is shown in Fig 10a. The region where the two limit cycles coexist is highlighted in grey. Decreasing $C_{PV\to P_2}$ impacts all the bifurcations. For $C_{PV\to P_2} = 300$ (Fig 10b) and $\varphi_{e1} = 0$, all bifurcations shift slightly to the left, indicating that oscillatory activity occurs at lower levels of external inputs (hyperexcitability). The most affected bifurcation is the one related to gamma oscillations (HB_2^+, grey curve), whose shift significantly enlarges the grey-shaded area, implying that multifrequency activity is more easily achieved.

Further decreasing $C_{PV\to P_2}$ (which would correspond to increasing the cumulative damage caused by AβOs) reduces gamma activity, as shown in Fig 10(c). While the SNIC and HB_1^+ bifurcations shift further to the left, the HB_2^+ bifurcation shifts to the right, decreasing the grey-shaded area and, consequently, reducing the system's ability to exhibit multifrequency activity.

The results described above suggest that as AD progresses, the regime of co-existence of fast and slow oscillations is reduced, with fast oscillations being disrupted the most. This is important because there is a natural variance of mean

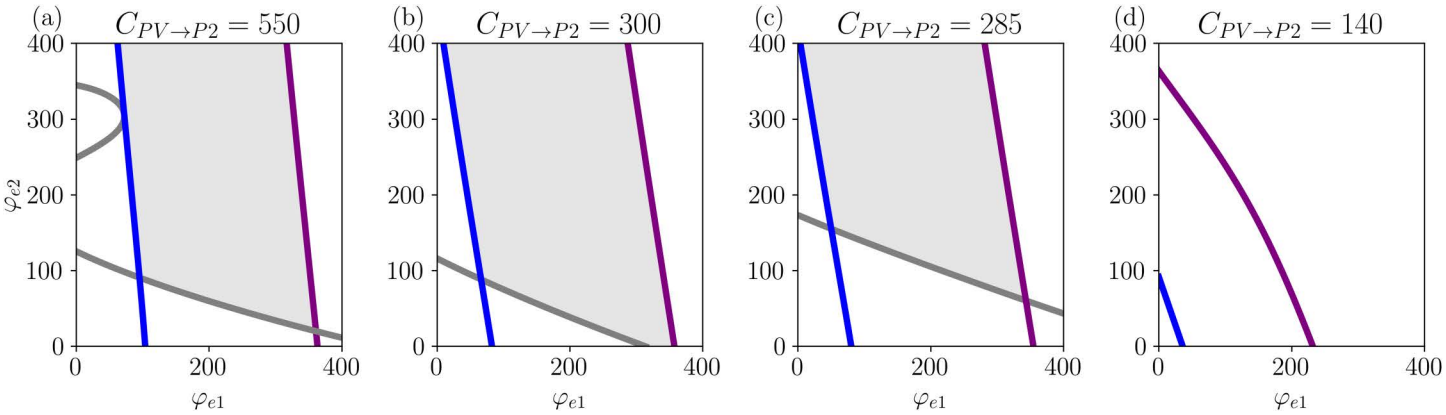

Fig 10. Bifurcation diagrams showing the effect of reducing $C_{PV\to P_2}$ on limit cycles and gamma activity. Panel (a) shows the baseline condition, while panels **(b)**–(d) illustrate the progressive reduction of multifrequency activity and the eventual extinction of gamma oscillations as $C_{PV\to P_2}$ decreases. The region where the two limit cycles coexist is highlighted in grey. Parameters as in Table 1.

https://doi.org/10.1371/journal.pcbi.1014022.g010

inputs to each (LaNMM) brain node as determined by dynamics and connectivity. Nodes with lower mean input to P1 and P2 will be affected first.

This observation aligns with the evidence on reduced gamma power in AD [50]. Thus, the model supports the idea that early-stage AD is primarily driven by an imbalance between excitation and inhibition driven by PV interneuron dysfunction [50,60,62,64]. Additionally, further reductions in $C_{PV\to P_2}$ result in the complete extinction of gamma oscillations in the LaNMM model, as shown in Fig 10d.

3.4 Long-range connectivity

So far, we have considered a model with short-range connections, where all possible external inputs due to long-range connections are encoded by the parameters φ_{e1} and φ_{e2}. In this section, we briefly investigate the impact of long-range connections on the dynamics of the model, particularly on its ability to sustain multifrequency activity. The coupling scheme between columns is based on the model proposed in [65] and supported by [66–68]. The final model is illustrated in Fig 11.

This model represents two cortical columns, each consisting of a LaNMM: superficial layers are modeled by the PING model, and a deep layers are modeled by the Jansen-Rit model. Long-range connections represent the connectivity between the two cortical columns and are divided into feedback and feed-forward projections. Feed-forward projections originate from the superficial layer in column 1 and target the superficial layer in column 2. Feedback projections originate from the deep layer in column 2 and target both superficial and deep layers in column 1. To encode this information we use two independent indices. The first index ($i = 1,2$) denotes the cortical column (1 = low-level area, 2 = high-level area). The second index (j = 1,2) denotes the layer within each column (1 = deep layer, 2 = superficial layer). Thus, P_{ij} refers to the population in column i and layer j (e.g., P_{12} = superficial population in the low-level column).

For simplicity, we assume that populations of the same type have identical parameters A and a across columns. We also consider that all four pyramidal populations receive the same external input, φ. The equations governing the final two-column model are provided in S1 Materials Two-column model. Building on the analysis from previous sections, we now examine how external inputs to the pyramidal populations influence the stability of fixed points and the occurrence of bifurcations focusing on the average membrane potentials of the pyramidal populations.

The results are presented in of Fig 12a and 12b for column 1 (low-level area) and in 12c and 12d for column 2 (high-level area). For each column, the superficial-layer population P_{i2} is shown in the top panels (12a,12c), while the deep-layer

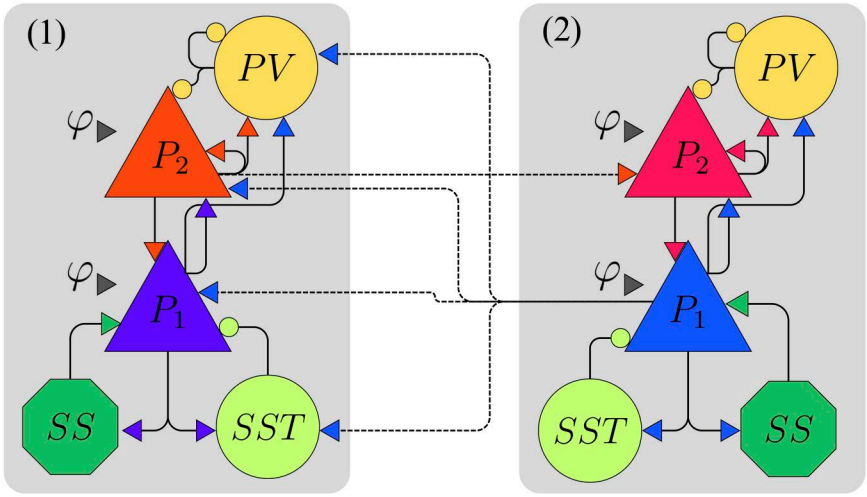

Fig 11. Illustration of the two-cortical-column model. Each column represents a laminar neural mass model. The two columns are coupled through feedback and feedforward connections and can receive external inputs. A detailed mathematical description of the model and the coupling equations is provided in S1 Two-column model.

https://doi.org/10.1371/journal.pcbi.1014022.g011

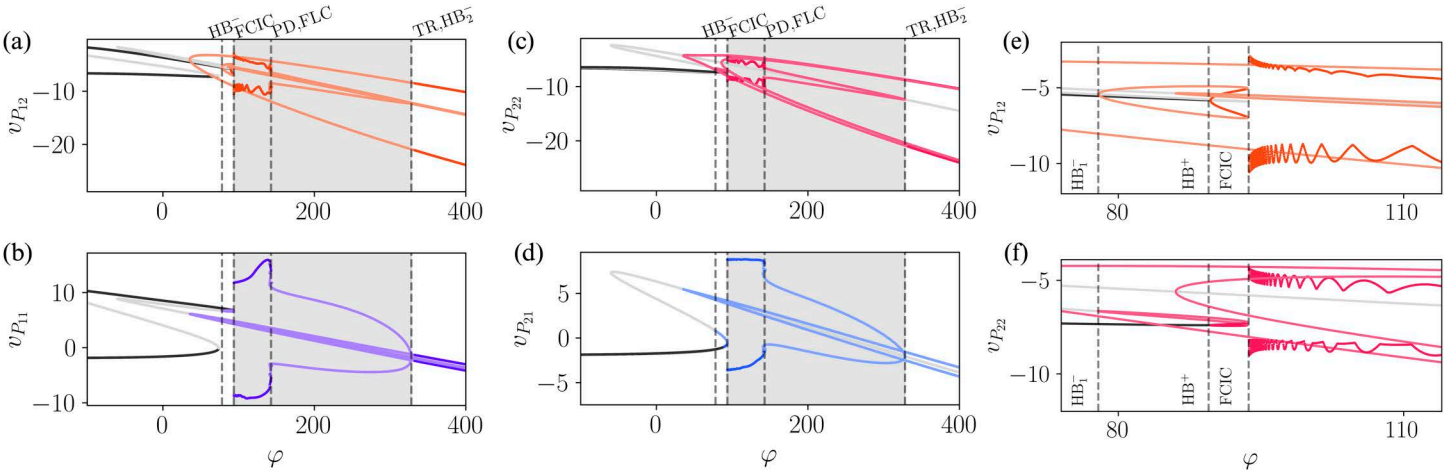

Fig 12. One parameter bifurcation diagram of the two cortical columns model. (a, b) One-parameter bifurcation diagrams for the oscillators of $v_{P_{11}}$ and $v_{P_{12}}$ as a function of φ. **(c, d)** Corresponding diagrams for $v_{P_{21}}$ and $v_{P_{22}}$ **(e,f)** Inset of the bifurcation diagrams from (a) and (b) highlighting in the region containing the FCIC bifurcation.

https://doi.org/10.1371/journal.pcbi.1014022.g012

population P_{i1} is shown in the bottom panels (12b,12d). Thus, the populations in column 1 are P_{11} (deep) and P_{12} (superficial), and those in column 2 are P_{21} (deep) and P_{22} (superficial). Insets of 12a and 12b are displayed in 12e and 12f, respectively. Although the introduction of coupling between columns increases the complexity of the system compared to the single-column model, leading to richer dynamical behavior, the bifurcation scenario still bears an important resemblance with the one of Fig 6: the coexistence of multiple limit cycles.

Before the emergence of any limit cycle in the bifurcation diagrams of Fig 12, we notice that the system exhibits one additional stable fixed point compared to the original model, leading to bistability. The emergence of the first limit cycle happens at $\varphi \approx 35$ through an HB_1^- bifurcation at $\varphi \approx 35$, which is unstable until it goes through a TR bifurcation around

$\varphi \approx 332$. Further increasing φ leads to another HB^- near $\varphi \approx 86$, where an unstable limit cycle emerges. This is followed by an HB^+, associated with a stable limit cycle, as shown in Fig 12e and 12f. These two limit cycles collide in a fold of cycles bifurcation (FCIC), giving rise to a stable limit cycle. Once again, the system's main frequency remains below α, while the P_2 populations exhibit a γ component, which allows $\delta - \gamma$ and $\theta - \gamma$ couplings. As φ continues to increase, the system undergoes a series of period-doubling (PD) and FLC bifurcations around $\varphi \approx 142$. Following these transitions, both columns exhibit $\alpha - \gamma$ coupling. The multifrequency activity ceases when the limit cycle originating from the FCIC bifurcation disappears in an HB_2^- near the TR bifurcation. Beyond this point, both columns oscillate solely at the γ frequency.

The asymmetry in the coupling causes the dynamics of the populations in different columns to differ. For instance, compared to the original model, P_{11} receives an extra input from P_{21}, and two populations projecting into P_{11} (P_{12} and SST_{11}) also receives an input from P_{21}. Across the range of φ studied, P_{11} exhibits a larger amplitude than P_{21}, which reflects the larger number of pyramidal neurons being activated in P_{11}. For the top layer pyramidal populations, P_{12} and P_{22}, although the amplitudes are similar, the dynamics for the range between the SNIC and the FLC bifurcations is rather different.

The time evolution of the membrane potentials is shown in Fig 13. The top row displays the dynamics of $v_{P_{11}}$ and $v_{P_{21}}$, while the bottom row shows $v_{P_{12}}$ and $v_{P_{22}}$. As the external input φ increases from $\varphi = 100$ (a–b) to $\varphi = 125$ (c–d) and $\varphi = 190$ (e–f), the activity of the P_1 populations shifts from the delta to the alpha frequency band. A similar trend is observed in $v_{P_{12}}$ and $v_{P_{22}}$, although with a more pronounced gamma component. This indicates that while the coupling between columns adds complexity to the model, as observed in the bifurcation diagram, the core feature of the model remains robust and is governed by the same mechanism: the coexistence of limit cycles.

4 Discussion

In this paper we investigate the dynamical properties of a laminar neural mass model, designed to capture different dynamics across cortical layers. The model achieves this by combining two neural mass models, each exhibiting oscillatory dynamics in distinct natural frequency bands, meaning that under external perturbations, each component oscillates at different frequencies. As in the original work, we consider that both pyramidal populations are targeted by external inputs φ_{e1} and φ_{e2}. To analyze the system's behavior, we first use φ_{e1} as the bifurcation parameter while keeping $\varphi_{e2} = 0$, allowing us to examine its role in triggering oscillatory dynamics. As shown in Fig 5, the oscillatory regime can be divided

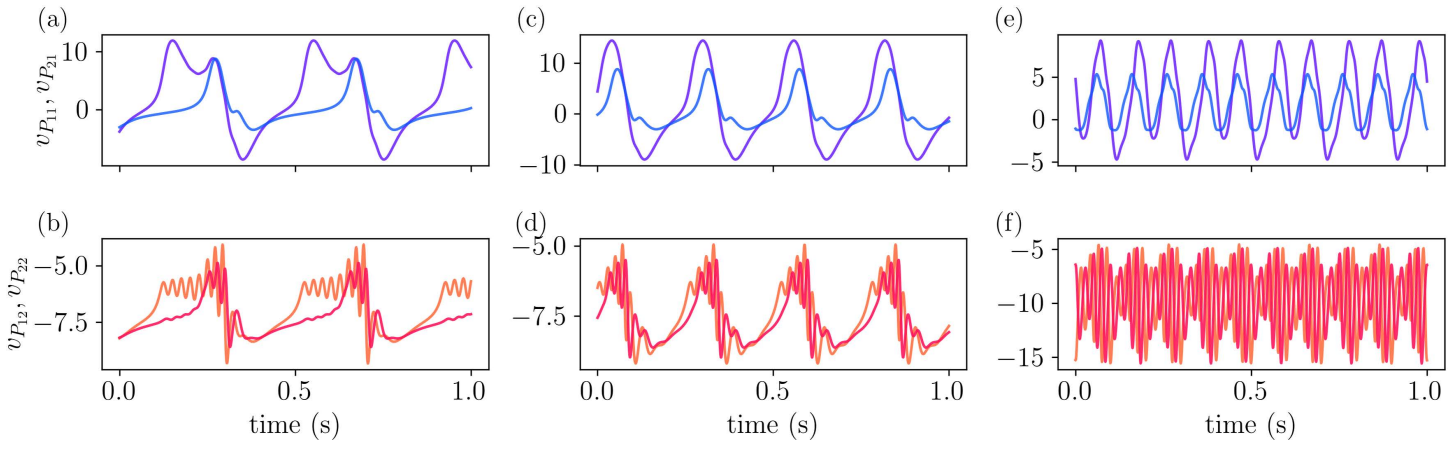

Fig 13. Time evolution of membrane potentials in the two-column model. Top row: Dynamics of $v_{P_{11}}$ and $v_{P_{21}}$ as the external input φ increases, illustrating a transition from delta to alpha frequency bands. Bottom row: Corresponding dynamics of $v_{P_{12}}$ and $v_{P_{22}}$, showing similar trends but with a prominent gamma-band component. **(a–b)**: $\varphi = 100$; **(c–d)**: $\varphi = 125$; **(e–f)**: $\varphi = 190$.

https://doi.org/10.1371/journal.pcbi.1014022.g013

into three regions depending on the value of φ_{e1}, with the dominant frequency transitioning from θ to γ. Additionally, for intermediate values of φ_{e1}, the oscillatory behavior resembles that observed in the Jansen-Rit model, whereas for higher values, the activity accelerates, corresponding to a PING mechanism for gamma activity.

We also investigate the role of φ_{e2} in the emergence of rhythmic activity. This input directly targets the PING component of the model, and thus we expect it to facilitate the emergence of gamma oscillations. This is precisely what we observe in Fig 6: as we increase the value of φ_{e2}, the HB bifurcation that gives rise to gamma activity occurs at smaller values of φ_{e1}. This clarifies the mechanism behind the multifrequency activity observed in LaNMM: the coexistence of limit cycles, one sustaining low-frequency oscillations and the other supporting high-frequency oscillations. We verify the robustness of this mechanism through a two-parameter bifurcation analysis as a function of φ_{e1} and φ_{e2}, shown in Fig 7, where we observe a large region in the parameter space where the two limit cycles coexist.

Of particular interest are the regions delimited by the torus bifurcations (TR), where the system exhibits quasiperiodic dynamics, and both α and γ frequencies have significant power. Within this region, the model is capable of exhibiting multifrequency activity across different frequency ranges, including δ-γ, θ-γ, and α-γ. We conclude our analysis by evaluating the Lyapunov exponents of the model, shown in Fig 9. While quasiperiodicity is observed over a large area of the parameter space, we also identify periodic dynamics in regions where both limit cycles coexist. This behavior can be understood by considering the two layers of the model as entrained oscillators. In such scenarios, the oscillators can resonate, a phenomenon that gives rise to Arnold tongues. This is precisely what we observe in the regions of periodic activity. Moreover, we also observe chaos in small regions of the parameter space.

We highlight the significance of the region where the system exhibits two limit cycles by modeling PV interneuron dysfunction, recently proposed as a mechanism to represent AβO, a key biomarker of Alzheimer's disease progression. As PV cell connectivity deteriorates, the system gradually loses its ability to generate multifrequency activity and, in advanced cases, ceases to oscillate altogether. This suggests that as the disease progresses, the coexistence of fast and slow oscillations diminishes, with fast oscillations being the most affected, in line with the results in [50].

We also extended the model to account for long-range connectivity. By incorporating a feedforward and feedback coupling scheme between columns, we demonstrate that the coexistence of limit cycles persists under these conditions. This is confirmed through a bifurcation analysis of the extended model, as shown in Fig 12. As expected, this model exhibits a more complex bifurcation structure; however, more importantly, rhythmic activity emerges in both the bottom and top layers. As a result, multifrequency activity is observed in both columns at different frequency ranges, as illustrated in Fig 13.

We emphasize that the mechanism of coexisting limit cycles underlies the approach of incorporating different neural populations to account for multiple frequency ranges in neural mass models, a concept that is not new. The strength of the LaNMM model lies in its ability to exhibit diverse frequency couplings using only five neural populations, controlled solely by adjusting the level of external inputs. While previous models have also been capable of generating multiple frequency interactions, they typically required either increasing the number of neural populations or modifying the time constants of specific populations (a and φ_0 in our case) to access different frequency regimes [42,69,70]. This demonstrates the efficiency of LaNMM in capturing complex neural dynamics with a relatively simple yet powerful parametrization. In order to further refine the LaNMM, future work should generalize our formalism towards next-generation neural mass models [71]. This modeling framework provides additional equations, rigorously derived from microscopic dynamics, for each neural population mean firing-rate and membrane potential, to which the sigmoid function employed here represents a quasi-stationary approximation [71,72]. To the best of our knowledge, multifrequency activity in these models has been studied only for the case of external forcing [73], and two interacting inhibitory populations with different time scales [74].

Our analysis highlights the potential of the LaNMM to model various phenomena and different brain regions in future studies. The ability to exhibit multifrequency activity is a prerequisite for capturing cross-frequency coupling phenomena, such as phase–amplitude coupling (PAC) and amplitude–amplitude coupling (AAC), as well as other features commonly observed in neural recordings. For instance, the three frequency couplings observed here are also found in brain

activity: δ-γ coupling has been proposed as a biomarker of postictal activity [75] and is linked to dopamine modulation [76]; θ-γ coupling is observed in the hippocampus of both rodents and humans [77,78]; and α-γ coupling has been associated with cognitive processes [37,79,80]. Recent results show that the cross-frequency coupling exhibited by the LaNMM can provide the key mechanisms for predictive coding, gating [34] and cooperation/competition across brain regions [35].

Supporting information

S1 Material. This supporting document contains all supplementary equations and methods cited in the main text.
(PDF)

Author contributions

Conceptualization: Raul de Palma Aristides, Pau Clusella, Roser Sanchez-Todo, Giulio Ruffini, Jordi Garcia-Ojalvo.

Formal analysis: Raul de Palma Aristides, Pau Clusella.

Funding acquisition: Giulio Ruffini, Jordi Garcia-Ojalvo.

Investigation: Raul de Palma Aristides, Giulio Ruffini, Jordi Garcia-Ojalvo.

Methodology: Raul de Palma Aristides, Pau Clusella, Roser Sanchez-Todo.

Resources: Jordi Garcia-Ojalvo.

Software: Raul de Palma Aristides, Pau Clusella.

Supervision: Giulio Ruffini, Jordi Garcia-Ojalvo.

Validation: Raul de Palma Aristides.

Visualization: Raul de Palma Aristides.

Writing – original draft: Raul de Palma Aristides, Jordi Garcia-Ojalvo.

Writing – review & editing: Raul de Palma Aristides, Pau Clusella, Roser Sanchez-Todo, Giulio Ruffini, Jordi Garcia-Ojalvo.

References

1. Buzsáki G. Rhythms of the Brain. New York: Oxford University Press; 2006. https://doi.org/10.1093/acprof:oso/9780195301069.001.0001
2. Hutcheon B, Yarom Y. Resonance, oscillation and the intrinsic frequency preferences of neurons. Trends Neurosci. 2000;23(5):216–22. https://doi.org/10.1016/s0166-2236(00)01547-2 PMID: 10782127
3. Wilson MA, McNaughton BL. Reactivation of hippocampal ensemble memories during sleep. Science. 1994;265(5172):676–9. https://doi.org/10.1126/science.8036517 PMID: 8036517
4. Buzsáki G, Draguhn A. Neuronal oscillations in cortical networks. Science. 2004;304(5679):1926–9. https://doi.org/10.1126/science.1099745 PMID: 15218136
5. Wilson HR, Cowan JD. Excitatory and inhibitory interactions in localized populations of model neurons. Biophys J. 1972;12(1):1–24. https://doi.org/10.1016/S0006-3495(72)86068-5 PMID: 4332108
6. Freeman WJ. Mass action in the nervous system. Elsevier; 1975. https://doi.org/10.1016/c2009-0-03145-6
7. Jansen BH, Zouridakis G, Brandt ME. A neurophysiologically-based mathematical model of flash visual evoked potentials. Biol Cybern. 1993;68(3):275–83. https://doi.org/10.1007/BF00224863 PMID: 8452897
8. Jansen BH, Rit VG. Electroencephalogram and visual evoked potential generation in a mathematical model of coupled cortical columns. Biol Cybern. 1995;73(4):357–66. https://doi.org/10.1007/BF00199471 PMID: 7578475
9. Montbrió E, Pazó D, Roxin A. Macroscopic description for networks of spiking neurons. Physical Review X. 2015;5:021028.
10. Buzsáki G, Anastassiou CA, Koch C. The origin of extracellular fields and currents--EEG, ECoG, LFP and spikes. Nat Rev Neurosci. 2012;13(6):407–20. https://doi.org/10.1038/nrn3241 PMID: 22595786
11. Wendling F, Bartolomei F, Bellanger JJ, Chauvel P. Epileptic fast activity can be explained by a model of impaired GABAergic dendritic inhibition. Eur J Neurosci. 2002;15(9):1499–508. https://doi.org/10.1046/j.1460-9568.2002.01985.x PMID: 12028360

12. David O, Friston KJ. A neural mass model for MEG/EEG: coupling and neuronal dynamics. Neuroimage. 2003;20(3):1743–55. https://doi.org/10.1016/j.neuroimage.2003.07.015 PMID: 14642484
13. Deco G, Jirsa VK, Robinson PA, Breakspear M, Friston K. The dynamic brain: from spiking neurons to neural masses and cortical fields. PLoS Comput Biol. 2008;4(8):e1000092. https://doi.org/10.1371/journal.pcbi.1000092 PMID: 18769680
14. Coombes S. Large-scale neural dynamics: simple and complex. Neuroimage. 2010;52(3):731–9. https://doi.org/10.1016/j.neuroimage.2010.01.045 PMID: 20096791
15. Pons AJ, Cantero JL, Atienza M, Garcia-Ojalvo J. Relating structural and functional anomalous connectivity in the aging brain via neural mass modeling. Neuroimage. 2010;52(3):848–61. https://doi.org/10.1016/j.neuroimage.2009.12.105 PMID: 20056154
16. Pinotsis D, Robinson P, Beim Graben P, Friston K. Neural masses and fields: modeling the dynamics of brain activity. Front Comput Neurosci. 2014;8:149. https://doi.org/10.3389/fncom.2014.00149 PMID: 25477813
17. Jedynak M, Pons AJ, Garcia-Ojalvo J, Goodfellow M. Temporally correlated fluctuations drive epileptiform dynamics. Neuroimage. 2017;146:188–96. https://doi.org/10.1016/j.neuroimage.2016.11.034 PMID: 27865920
18. Jedynak M, Pons AJ, Garcia-Ojalvo J. Collective excitability in a mesoscopic neuronal model of epileptic activity. Phys Rev E. 2018;97(1–1):012204. https://doi.org/10.1103/PhysRevE.97.012204 PMID: 29448445
19. Köksal Ersöz E, Modolo J, Bartolomei F, Wendling F. Neural mass modeling of slow-fast dynamics of seizure initiation and abortion. PLoS Comput Biol. 2020;16(11):e1008430. https://doi.org/10.1371/journal.pcbi.1008430 PMID: 33166277
20. Deschle N, Ignacio Gossn J, Tewarie P, Schelter B, Daffertshofer A. On the Validity of Neural Mass Models. Front Comput Neurosci. 2021;14:581040. https://doi.org/10.3389/fncom.2020.581040 PMID: 33469424
21. Griffiths JD, Bastiaens SP, Kaboodvand N. Whole-brain modelling: Past, present, and future. In: Giugliano M, Negrello M, Linaro D, editors. Computational Modelling of the Brain. Cham: Springer; 2022. https://doi.org/10.1007/978-3-030-89439-9_13
22. Sanchez-Todo R, Bastos AM, Lopez-Sola E, Mercadal B, Santarnecchi E, Miller EK, et al. A physical neural mass model framework for the analysis of oscillatory generators from laminar electrophysiological recordings. Neuroimage. 2023;270:119938. https://doi.org/10.1016/j.neuroimage.2023.119938 PMID: 36775081
23. Forrester M, Petros S, Cattell O, Lai YM, O'Dea RD, Sotiropoulos S, et al. Whole brain functional connectivity: Insights from next generation neural mass modelling incorporating electrical synapses. PLoS Comput Biol. 2024;20(12):e1012647. https://doi.org/10.1371/journal.pcbi.1012647 PMID: 39637233
24. Clusella P, Deco G, Kringelbach ML, Ruffini G, Garcia-Ojalvo J. Complex spatiotemporal oscillations emerge from transverse instabilities in large-scale brain networks. PLoS Comput Biol. 2023;19(4):e1010781. https://doi.org/10.1371/journal.pcbi.1010781 PMID: 37043504
25. Ruffini G, Sanchez-Todo R, Dubreuil L, Salvador R, Pinotsis D, Miller EK, et al. P118 A Biophysically realistic Laminar Neural Mass Modeling framework for transcranial Current Stimulation. Clin Neurophysiol. 2020;131(4):e78–9. https://doi.org/10.1016/j.clinph.2019.12.229
26. Ward LM. Synchronous neural oscillations and cognitive processes. Trends Cogn Sci. 2003;7(12):553–9. https://doi.org/10.1016/j.tics.2003.10.012 PMID: 14643372
27. Maier A, Adams GK, Aura C, Leopold DA. Distinct superficial and deep laminar domains of activity in the visual cortex during rest and stimulation. Front Syst Neurosci. 2010;4:31. https://doi.org/10.3389/fnsys.2010.00031 PMID: 20802856
28. Buffalo EA, Fries P, Landman R, Buschman TJ, Desimone R. Laminar differences in gamma and alpha coherence in the ventral stream. Proc Natl Acad Sci U S A. 2011;108(27):11262–7. https://doi.org/10.1073/pnas.1011284108 PMID: 21690410
29. Spaak E, Bonnefond M, Maier A, Leopold DA, Jensen O. Layer-specific entrainment of γ-band neural activity by the α rhythm in monkey visual cortex. Curr Biol. 2012;22(24):2313–8. https://doi.org/10.1016/j.cub.2012.10.020 PMID: 23159599
30. Ninomiya T, Dougherty K, Godlove DC, Schall JD, Maier A. Microcircuitry of agranular frontal cortex: contrasting laminar connectivity between occipital and frontal areas. J Neurophysiol. 2015;113(9):3242–55. https://doi.org/10.1152/jn.00624.2014 PMID: 25744881
31. Bastos AM, Vezoli J, Bosman CA, Schoffelen J-M, Oostenveld R, Dowdall JR, et al. Visual areas exert feedforward and feedback influences through distinct frequency channels. Neuron. 2015;85(2):390–401. https://doi.org/10.1016/j.neuron.2014.12.018 PMID: 25556836
32. Bonaiuto JJ, Meyer SS, Little S, Rossiter H, Callaghan MF, Dick F, et al. Lamina-specific cortical dynamics in human visual and sensorimotor cortices. Elife. 2018;7:e33977. https://doi.org/10.7554/eLife.33977 PMID: 30346274
33. Johnston K, Ma L, Schaeffer L, Everling S. Alpha Oscillations Modulate Preparatory Activity in Marmoset Area 8Ad. J Neurosci. 2019;39(10):1855–66. https://doi.org/10.1523/JNEUROSCI.2703-18.2019 PMID: 30651331
34. Ruffini G, et al. Cross-frequency coupling as a neural substrate for predictive coding: A laminar neural mass modeling approach. In: 2025. https://doi.org/10.1101/2025.03.19.644090
35. Mercadal B, et al. Bridging local and global dynamics: a laminar mechanistic model for cooperative and competitive interactions in the brain. bioRxiv. 2025. https://doi.org/10.1101/2025.07.09.663817
36. Xing D, Yeh C-I, Burns S, Shapley RM. Laminar analysis of visually evoked activity in the primary visual cortex. Proc Natl Acad Sci U S A. 2012;109(34):13871–6. https://doi.org/10.1073/pnas.1201478109 PMID: 22872866
37. Bastos AM, Loonis R, Kornblith S, Lundqvist M, Miller EK. Laminar recordings in frontal cortex suggest distinct layers for maintenance and control of working memory. Proc Natl Acad Sci U S A. 2018;115(5):1117–22. https://doi.org/10.1073/pnas.1710323115 PMID: 29339471

38. Chen CC, Kiebel SJ, Friston KJ. Dynamic causal modelling of induced responses. Neuroimage. 2008;41(4):1293–312. https://doi.org/10.1016/j.neuroimage.2008.03.026 PMID: 18485744
39. Jirsa V, Müller V. Cross-frequency coupling in real and virtual brain networks. Front Comput Neurosci. 2013;7:78. https://doi.org/10.3389/fncom.2013.00078 PMID: 23840188
40. Onslow ACE, Jones MW, Bogacz R. A canonical circuit for generating phase-amplitude coupling. PLoS One. 2014;9(8):e102591. https://doi.org/10.1371/journal.pone.0102591 PMID: 25136855
41. Hyafil A, Giraud A-L, Fontolan L, Gutkin B. Neural Cross-Frequency Coupling: Connecting Architectures, Mechanisms, and Functions. Trends Neurosci. 2015;38(11):725–40. https://doi.org/10.1016/j.tins.2015.09.001 PMID: 26549886
42. Sotero RC. Topology, Cross-Frequency, and Same-Frequency Band Interactions Shape the Generation of Phase-Amplitude Coupling in a Neural Mass Model of a Cortical Column. PLoS Comput Biol. 2016;12(11):e1005180. https://doi.org/10.1371/journal.pcbi.1005180 PMID: 27802274
43. Painchaud V, Doyon N, Desrosiers P. Beyond Wilson-Cowan dynamics: oscillations and chaos without inhibition. Biol Cybern. 2022;116(5–6):527–43. https://doi.org/10.1007/s00422-022-00941-w PMID: 36063212
44. Grimbert F, Faugeras O. Bifurcation analysis of Jansen's neural mass model. Neural Comput. 2006;18(12):3052–68. https://doi.org/10.1162/neco.2006.18.12.3052 PMID: 17052158
45. Leung LS. Nonlinear feedback model of neuronal populations in hippocampal CAl region. J Neurophysiol. 1982;47(5):845–68. https://doi.org/10.1152/jn.1982.47.5.845 PMID: 7086472
46. Traub RD, Jefferys JG, Whittington MA. Simulation of gamma rhythms in networks of interneurons and pyramidal cells. J Comput Neurosci. 1997;4(2):141–50. https://doi.org/10.1023/a:1008839312043 PMID: 9154520
47. Molaee-Ardekani B, Benquet P, Bartolomei F, Wendling F. Computational modeling of high-frequency oscillations at the onset of neocortical partial seizures: from "altered structure" to "dysfunction". Neuroimage. 2010;52(3):1109–22. https://doi.org/10.1016/j.neuroimage.2009.12.049 PMID: 20034581
48. Palop JJ, Mucke L. Network abnormalities and interneuron dysfunction in Alzheimer disease. Nat Rev Neurosci. 2016;17(12):777–92. https://doi.org/10.1038/nrn.2016.141 PMID: 27829687
49. Gendra JC, et al. Restoring oscillatory dynamics in Alzheimer's disease: A laminar whole-brain model of serotonergic psychedelic effects. 2024. https://doi.org/10.1101/2024.12.15.628565
50. Roser Sanchez-Todo, et al. Fast interneuron dysfunction in laminar neural mass model reproduces Alzheimer's oscillatory biomarkers. bioRxiv. 2025.
51. Lopes da Silva FH, Hoeks A, Smits H, Zetterberg LH. Model of brain rhythmic activity. Kybernetik. 1974;15(1):27–37. https://doi.org/10.1007/bf00270757
52. van Rotterdam A, Lopes da Silva FH, van den Ende J, Viergever MA, Hermans AJ. A model of the spatial-temporal characteristics of the alpha rhythm. Bull Math Biol. 1982;44(2):283–305. https://doi.org/10.1007/BF02463252 PMID: 7074252
53. Kandel ER, et al. Principles of Neural Science. Vol. 4. New York: McGraw-Hill; 2000.
54. Fourier transform property. Using $F[te^{-at}u(t)]=1/(a+j\omega)^2$ and linearity gives $H(j\omega)=Aa/(a+j\omega)^2$.
55. Lopes da Silva FH, van Rotterdam A, Barts P, van Heusden E, Burr W. Models of neuronal populations: the basic mechanisms of rhythmicity. Prog Brain Res. 1976;45:281–308. https://doi.org/10.1016/S0079-6123(08)60995-4 PMID: 1013341
56. Freeman WJ. Simulation of chaotic EEG patterns with a dynamic model of the olfactory system. Biol Cybern. 1987;56(2–3):139–50. https://doi.org/10.1007/BF00317988 PMID: 3593783
57. Doedel EJ, et al. AUTO-07P: Continuation and bifurcation software for ordinary differential equations. 2007. http://indy.cs.concordia.ca/auto/
58. Bifurcations of limit-cycles. This result can be reproduced using the code available in our repository. Note similar to Fig 1b of Ref. 24.
59. Tort ABL, Komorowski R, Eichenbaum H, Kopell N. Measuring phase-amplitude coupling between neuronal oscillations of different frequencies. J Neurophysiol. 2010;104(2):1195–210. https://doi.org/10.1152/jn.00106.2010 PMID: 20463205
60. Chung H, Park K, Jang HJ, Kohl MM, Kwag J. Dissociation of somatostatin and parvalbumin interneurons circuit dysfunctions underlying hippocampal theta and gamma oscillations impaired by amyloid β oligomers in vivo. Brain Struct Funct. 2020;225(3):935–54. https://doi.org/10.1007/s00429-020-02044-3 PMID: 32107637
61. Park K, et al. Optogenetic activation of parvalbumin and somatostatin interneurons selectively restores theta-nested gamma oscillations… impaired by amyloid β oligomers. BMC Biol. 2020;18(1):7. https://doi.org/10.1186/s12915-019-0732-7
62. Garcia-Marin V, Blazquez-Llorca L, Rodriguez J-R, Boluda S, Muntane G, Ferrer I, et al. Diminished perisomatic GABAergic terminals on cortical neurons adjacent to amyloid plaques. Front Neuroanat. 2009;3:28. https://doi.org/10.3389/neuro.05.028.2009 PMID: 19949482
63. Martinez-Losa M, Tracy TE, Ma K, Verret L, Clemente-Perez A, Khan AS, et al. Nav1.1-Overexpressing Interneuron Transplants Restore Brain Rhythms and Cognition in a Mouse Model of Alzheimer's Disease. Neuron. 2018;98(1):75–89.e5. https://doi.org/10.1016/j.neuron.2018.02.029 PMID: 29551491
64. Verret L, Mann EO, Hang GB, Barth AMI, Cobos I, Ho K, et al. Inhibitory interneuron deficit links altered network activity and cognitive dysfunction in Alzheimer model. Cell. 2012;149(3):708–21. https://doi.org/10.1016/j.cell.2012.02.046 PMID: 22541439

65. Rabasa AC. Long-range brain connectivity and its role in brain network modeling. MA thesis. UPC. 2024.
66. Mejias JF, Murray JD, Kennedy H, Wang X-J. Feedforward and feedback frequency-dependent interactions in a large-scale laminar network of the primate cortex. Sci Adv. 2016;2(11):e1601335. https://doi.org/10.1126/sciadv.1601335 PMID: 28138530
67. Jaramillo J, Mejias JF, Wang X-J. Engagement of Pulvino-cortical Feedforward and Feedback Pathways in Cognitive Computations. Neuron. 2019;101(2):321-336.e9. https://doi.org/10.1016/j.neuron.2018.11.023 PMID: 30553546
68. Wang X-J. Theory of the Multiregional Neocortex: Large-Scale Neural Dynamics and Distributed Cognition. Annu Rev Neurosci. 2022;45:533–60. https://doi.org/10.1146/annurev-neuro-110920-035434 PMID: 35803587
69. Chehelcheraghi M, Nakatani C, Steur E, van Leeuwen C. A neural mass model of phase–amplitude coupling. Biol Cybern. 2016;110(2–3):171–92. https://doi.org/10.1007/s00422-016-0687-5
70. Chehelcheraghi M, van Leeuwen C, Steur E, Nakatani C. A neural mass model of cross frequency coupling. PLoS One. 2017;12(4):e0173776. https://doi.org/10.1371/journal.pone.0173776 PMID: 28380064
71. Devalle F, Roxin A, Montbrió E. Firing rate equations require a spike synchrony mechanism to correctly describe fast oscillations in inhibitory networks. PLoS Comput Biol. 2017;13(12):e1005881. https://doi.org/10.1371/journal.pcbi.1005881 PMID: 29287081
72. Clusella P, Köksal-Ersöz E, Garcia-Ojalvo J, Ruffini G. Comparison between an exact and a heuristic neural mass model with second-order synapses. Biol Cybern. 2023;117(1–2):5–19. https://doi.org/10.1007/s00422-022-00952-7 PMID: 36454267
73. Segneri M, Bi H, Olmi S, Torcini A. Theta-Nested Gamma Oscillations in Next Generation Neural Mass Models. Front Comput Neurosci. 2020;14:47. https://doi.org/10.3389/fncom.2020.00047 PMID: 32547379
74. Ceni A, Olmi S, Torcini A, Angulo-Garcia D. Cross frequency coupling in next generation inhibitory neural mass models. Chaos. 2020;30(5):053121. https://doi.org/10.1063/1.5125216 PMID: 32491891
75. Grigorovsky V, Jacobs D, Breton VL, Tufa U, Lucasius C, Del Campo JM, et al. Delta-gamma phase-amplitude coupling as a biomarker of postictal generalized EEG suppression. Brain Commun. 2020;2(2):fcaa182. https://doi.org/10.1093/braincomms/fcaa182 PMID: 33376988
76. Andino-Pavlovsky V, Souza AC, Scheffer-Teixeira R, Tort ABL, Etchenique R, Ribeiro S. Dopamine Modulates Delta-Gamma Phase-Amplitude Coupling in the Prefrontal Cortex of Behaving Rats. Front Neural Circuits. 2017;11:29. https://doi.org/10.3389/fncir.2017.00029 PMID: 28536507
77. Buzsáki G, Buhl DL, Harris KD, Csicsvari J, Czéh B, Morozov A. Hippocampal network patterns of activity in the mouse. Neuroscience. 2003;116(1):201–11. https://doi.org/10.1016/s0306-4522(02)00669-3 PMID: 12535953
78. Canolty RT, Edwards E, Dalal SS, Soltani M, Nagarajan SS, Kirsch HE, et al. High gamma power is phase-locked to theta oscillations in human neocortex. Science. 2006;313(5793):1626–8. https://doi.org/10.1126/science.1128115 PMID: 16973878
79. Voytek B, Canolty RT, Shestyuk A, Crone NE, Parvizi J, Knight RT. Shifts in gamma phase-amplitude coupling frequency from theta to alpha over posterior cortex during visual tasks. Front Hum Neurosci. 2010;4:191. https://doi.org/10.3389/fnhum.2010.00191 PMID: 21060716
80. Park H, Lee DS, Kang E, Kang H, Hahm J, Kim JS, et al. Formation of visual memories controlled by gamma power phase-locked to alpha oscillations. Sci Rep. 2016;6:28092. https://doi.org/10.1038/srep28092 PMID: 27306959